
# Integrated microcavity optomechanics with a suspended photonic crystal mirror above a distributed Bragg reflector

Research Article | Vol. 31, No. 19 / 11 Sep 2023 / Optics Express 30212
Optics EXPRESS

# Integrated microcavity optomechanics with a suspended photonic crystal mirror above a distributed Bragg reflector

Sushanth Kini Manjeshwar,[1,†] Anastasiia Ciers,[1,†] Juliette Monsel,[1,†] Hannes Pfeifer,[1] Cindy Peralle,[2] Shu Min Wang,[1] Philippe Tassin,[2] and Witlef Wieczorek[1,*]

[1]Department of Microtechnology and Nanoscience, Chalmers University of Technology, SE-412 96 Göteborg, Sweden
[2]Department of Physics, Chalmers University of Technology, SE-412 96 Göteborg, Sweden
[†]Authors with equal contribution
[*]witlef.wieczorek@chalmers.se

**Abstract:** Increasing the interaction between light and mechanical resonators is an ongoing endeavor in the field of cavity optomechanics. Optical microcavities allow for boosting the interaction strength through their strong spatial confinement of the optical field. In this work, we follow this approach by realizing a sub-wavelength-long, free-space optomechanical microcavity on-chip fabricated from an (Al,Ga)As heterostructure. A suspended GaAs photonic crystal mirror is acting as a highly reflective mechanical resonator, which together with a distributed Bragg (DBR) reflector forms an optomechanical microcavity. We demonstrate precise control over the microcavity resonance by change of the photonic crystal parameters. We find that the microcavity mode can strongly couple to the transmissive modes of the DBR. The interplay between the microcavity mode and a guided resonance of the photonic crystal modifies the cavity response and results in a stronger dynamical backaction on the mechanical resonator compared to conventional optomechanical dynamics.



## 1. Introduction

Optical microcavities [1] confine light to small mode volumes leading to stronger light-matter interactions. As a consequence, microcavities have been used in various fields, including cavity QED [2–4], nonlinear optics [5,6], or vertical-cavity surface-emitting lasers [7,8]. Microcavities also find applications in the field of cavity optomechanics [9], which explores the interaction between a cavity mode and a mechanical resonator. Optomechanical microcavities have enabled demonstrations such as ground-state cooling of mechanical motion [10,11], coherent optomechanical coupling [12,13], and thermally driven nonlinear optomechanics [14].

Optomechanical microcavities can be categorized into two different topologies. Firstly, light can be confined fully within the material, i.e., in the plane of the device layer, as is the case with optomechanical crystals [15,16], whispering gallery mode resonators [17,18], or photonic crystal defect cavities [19]. Alternatively, light can be confined in free space, i.e., out-of-plane, by use of highly reflecting mirrors such as in Fabry-Perot-type microcavities [20–22]. While the former implementations allow for on-chip integration, inherent mechanical stability, and microfabrication flexibility, they may suffer from optical absorption [23]. The latter implementations circumvent this caveat but lack microfabrication flexibility and intrinsic mechanical stability.

In our work, we realize a high-quality optomechanical microcavity by combining in-plane and out-of-plane light propagation. We confine light to a sub-$\mu$m microcavity mode formed between

#496447 https://doi.org/10.1364/OE.496447
Journal © 2023 Received 25 May 2023; revised 6 Jul 2023; accepted 28 Jul 2023; published 29 Aug 2023

Optics EXPRESS

a distributed Bragg reflector (DBR) and a suspended photonic crystal (PhC) mirror. Our PhC-DBR microcavity combines the advantages of inherent mechanical stability realized through a single-lithography microfabrication process from an (Al,Ga)As heterostructure [24] with on-chip scalability and flexibility over design parameters. The reflection of the PhC mirror is determined by the Fano interference between out-of-plane and in-plane light modes and can be engineered to obtain a reflectivity approaching unity [25]. At the same time, the suspended PhC mirror acts as the mechanical resonator [24,26–28] of the optomechanical cavity. Suspended PhC mirrors have been used in cavity optomechanical systems, such as for an optomechanical microcavity exhibiting both photothermal and optomechanical effects [29,30], as membrane-in-the-middle cavity optomechanical systems [31,32], as photonic crystal cavities [33,34] or defect cavities [19]. Furthermore, suspended PhC mirrors exhibit features for cavity optomechanical systems, which are not accessible by conventional mirrors, such as focusing capability [35], linewidth narrowing [36], or realization of photonic bound states in the continuum [37]. Interestingly, we find that the optical mode of the microcavity and transmission modes of the DBR couple strongly with each other, which may find new applications in cavity optomechanics.

In our PhC-based optomechanical microcavity, we observe a stronger dynamical backaction compared to canonical cavity optomechanics. This stronger interaction originates from the interplay between the microcavity mode and a guided resonance of the photonic crystal [25], which was analyzed in Refs. [36,38]. We extend that analysis by incorporating dispersive coupling of the guided resonance of the suspended PhC to its mechanical motion. Moreover, we also account for dissipative coupling of the optical modes to the motion of the suspended PhC [19,39,40].

In the following, we present the fabrication of the optomechanical microcavity from an (Al,Ga)As heterostructure. We summarize the theory required to describe the optical and optomechanical properties of our microcavity. We then characterize the optical reflectivity of the microcavity and demonstrate the tunability of the cavity resonance wavelength by variation of the PhC hole radius. Finally, we characterize the mechanical properties of the suspended PhC reflector and their tunability through the use of cavity optomechanical effects, which deviate considerably from the expected optical spring effect in non-sideband resolved canonical optomechanics [9].

## 2. Experimental methods

### 2.1. Device fabrication

The optomechanical microcavity is fabricated from an (Al,Ga)As heterostructure, which is grown on a GaAs substrate using molecular beam epitaxy. Note that the GaAs substrate is not back-polished, which prevents us from measuring transmission through the entire device. This monolithic assembly avoids post-alignment of optical mirrors forming a microcavity and also active cavity length stabilization, which is required, for instance, in fiber-based microcavities [41,42]. The as-grown heterostructure [Fig. 1(a)] consists of a DBR mirror with 30 alternating layers of 106 nm-thick GaAs and 130 nm-thick $Al_{0.92}Ga_{0.08}As$ with a targeted reflectivity of 99.999% at 1480 nm. The DBR is followed by a 750 nm-thick $Al_{0.67}Ga_{0.33}As$ sacrificial layer, which determines the geometric length $L_g$ of the microcavity. On top of this sacrificial layer, a 95 nm-thick GaAs layer is grown as the device layer (thicknesses of the as-grown structure are inferred from transmission electron microscopy, see Supplement 1). The device layer is patterned with a PhC to increase its out-of-plane reflectivity in the telecom wavelength regime [24–26]. Standard microfabrication techniques were used to pattern the PhC into the GaAs device layer and to release it [24]. A scanning electron microscope (SEM) image of a fabricated device is shown in Fig. 1(b). The suspended PhC membrane together with the DBR mirror form a microcavity with a length $\approx \lambda/2$. Figure 1(c,d) present the electric field distribution of the

Optics EXPRESS

microcavity eigenmode obtained from a finite element method (FEM) simulation that clearly shows the field concentration between the PhC and DBR mirrors.

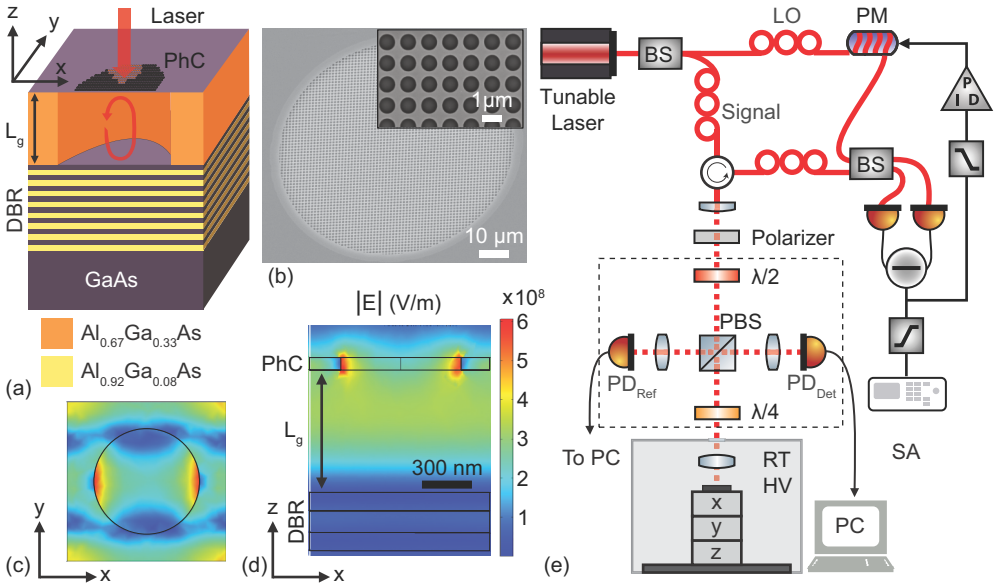


**Fig. 1.** (a) Schematic of a microcavity formed by a suspended photonic crystal (PhC) mirror and a distributed Bragg reflector (DBR) mirror monolithically fabricated from an (Al,Ga)As heterostructure. (b) SEM image of a suspended PhC membrane with a diameter of 70 $\mu$m. (c,d) FEM simulation of the electric field $|E|$ of the microcavity mode at a resonant wavelength of 1497 nm assuming linear input polarization. Note that due to the 4-fold rotational symmetry of the microcavity in the xy plane, the electric field for the orthogonal input polarization would be rotated by 90° around the z-axis. (e) Experimental setup used for characterizing the optomechanical properties of the microcavity. Red solid lines represent fiber beam paths and red dashed lines free-space beam paths. Dashed rectangle: optional reflection measurement setup, BS: beam splitter, PBS: polarizing beam splitter, PM: fiber-based phase modulator, SA: spectrum analyzer, $PD_{Ref(Det)}$: photodiode in the reference (detection) arm, RT: room temperature, HV: high vacuum of $5 \cdot 10^{-5}$ mbar.

### 2.2. *Experimental setup*

The characterization of the microcavity is performed with a tunable diode laser in the telecom wavelength regime (1480 nm to 1620 nm) using the setup shown in Fig. 1(e). We use a standard optical homodyne detection scheme [43] at room temperature to characterize the (opto)mechanical properties of the suspended PhC membrane placed in a vacuum chamber ($5 \cdot 10^{-5}$ mbar). The output of the laser is split into a signal and a local oscillator (LO) arm. The signal arm is collimated to a free-space beam path and focused onto the microcavity that is placed inside a vacuum chamber on a *xyz*-translation stage. The focal waist is 10 $\mu$m, when not stated otherwise. The mechanical displacement of the suspended PhC membrane is mapped onto the quadratures of the reflected light beam. The reflected beam is mixed with the LO beam in a tunable fiber beam splitter, whose output is sent to a balanced photodiode (BPD). The electronic signal from the BPD is passed through a high-pass filter and sent to a spectrum analyzer for evaluating the mechanical properties of the PhC membrane. The low-pass filtered BPD signal is used to lock the interferometer by applying feedback to a fiber-based phase modulator. The reference photodiode $PD_{Ref}$ is used to maintain a constant power reaching the sample when tuning the laser wavelength.

Optics EXPRESS

For characterizing the optical reflectance of the microcavity, additional components can be introduced into the free-space beam path of the signal arm (marked by the dashed box in Fig. 1(e)). The circularly polarized input beam acquires a $\pi$-phase shift upon reflection on the microcavity and, thus, will be directed to $\mathrm{PD_{Det}}$ after passing through a quarter-wave plate and polarizing beam splitter. To account for the optical response of the utilized components, we perform an independent calibration measurement with a mirror of known reflectivity that is used to normalize the obtained optical reflectance spectra of the microcavity [24].

## 3. Theory

We briefly present the theoretical description of the optomechanical microcavity via coupled mode theory, which allows us to describe its optical and optomechanical properties. More details are found in the Supplement 1 and in Ref. [44].

The system, depicted in Fig. 2, consists of a suspended PhC mirror and a DBR mirror that form an optical microcavity. The DBR can be treated as a highly reflective mirror in the telecom range. Conversely, the optical response of a PhC mirror is generally highly wavelength dependent [25,36], which we capture by accounting for a PhC guided resonance. Therefore, we model the microcavity with two coupled optical modes [38]: a Fabry-Perot cavity mode of frequency $\omega_a$ with photon annihilation operator $\hat{a}$ and an internal PhC optical mode of frequency $\omega_d$ with photon annihilation operator $\hat{d}$. The Hamiltonian for the optical part of the setup reads

$$\hat{H}_{\mathrm{opt}} = \hbar\omega_a\hat{a}^\dagger\hat{a} + \hbar\omega_d\hat{d}^\dagger\hat{d} + \hbar\Lambda(\hat{a}^\dagger\hat{d} + \hat{a}\hat{d}^\dagger), \tag{1}$$

where $\Lambda$ is the coupling strength between the modes and where we made the rotating wave approximation and neglected the two-mode squeezing terms [38]. In addition, the cavity mode couples to the environments above (denoted with subscript 1) and below (denoted with subscript 2) the cavity, giving rise to the respective loss rates $\kappa_1$ and $\kappa_2$. The mirror mode also couples to environment 1 with loss rate $\gamma_d$ [38].

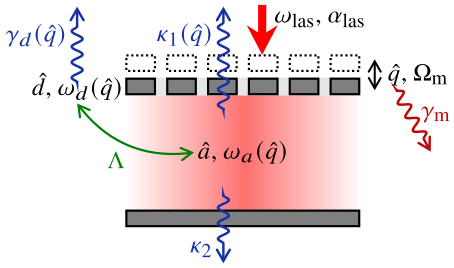


**Fig. 2.** Schematic of the optomechanical microcavity consisting of a suspended PhC mirror above a DBR. Symbols are explained in the main text.

The suspended PhC membrane acts as a mechanical resonator of frequency $\Omega_{\mathrm{m}}$ and position and momentum quadratures $\hat{q}$ and $\hat{p}$. The displacement of the suspended PhC membrane impacts the optical microcavity in various ways, resulting in different kinds of optomechanical couplings. First, the modulation of the Fabry-Perot cavity resonance frequency by the out-of-plane displacement of the PhC mirror creates the standard dispersive coupling, $g^0_{\omega,a}$. Second, we expect a dissipative coupling $g^0_{\kappa,a}$ of the Fabry-Perot mode. This dissipative coupling is specific to our microcavity implementation and its origin comes from the strong evanescent coupling between the optical modes $\hat{a}$ and $\hat{d}$ due to the short cavity length. When the cavity length changes due to the out-of-plane displacement of the PhC mirror, the evanescent coupling is modified, which affects the resonance frequency and optical loss rate of the microcavity, the latter resulting in dissipative coupling. Furthermore, we also take into account optomechanical couplings from the

Optics EXPRESS

interaction of the mechanical mode of the PhC with its guided optical mode $\hat{d}$. The out-of-plane displacement of the PhC results in an induced in-plane mechanical strain and displacement field impacting the PhC properties. As a result, the PhC mode $\hat{d}$ will have an altered frequency $\omega_d$ and linewidth $\gamma_d$. We model this by adding dispersive and dissipative optomechanical couplings between the PhC mode and the mechanics, respectively denoted $g^0_{\omega,d}$ and $g^0_{\kappa,d}$. We note that we do not model quadratic coupling of the mechanical quadratures to the light field as we do not observe a mechanical signal at twice the frequency in the measured mechanical noise power spectra.

As a result, the total Hamiltonian of the system is given by

$$\hat{H} = \hat{H}_{\text{opt}} + \frac{\hbar\Omega_{\text{m}}}{2}(\hat{q}^2 + \hat{p}^2) - \hbar g^0_{\omega,a}\sqrt{2}\hat{a}^\dagger\hat{a}\hat{q} - \hbar g^0_{\omega,d}\sqrt{2}\hat{d}^\dagger\hat{d}\hat{q}. \tag{2}$$

Furthermore, the cavity is driven by a laser of frequency $\omega_{\text{las}}$ and amplitude $\alpha_{\text{las}}$, and the mechanical resonator is coupled to a phonon bath, giving rise to the damping rate $\gamma_{\text{m}}$, so the dynamics of the whole system can be described, in the frame rotating at the laser frequency, by the following set of Langevin equations [38,44,45],

$$\begin{aligned}\dot{\hat{a}} = &-(i\Delta_a + \kappa)\hat{a} + \sqrt{2}(ig^0_{\omega,a} - g^0_{\kappa,a})\hat{q}\hat{a} - \mathcal{G}\hat{d} - \sqrt{2}g^{0,+}_{a,d}\hat{q}\hat{d} \\ &+ \left(\sqrt{2\kappa_1} + \frac{g^0_{\kappa,a}}{\sqrt{\kappa_1}}\hat{q}\right)(\alpha_{\text{las}} + \hat{a}_{\text{in},1}) + \sqrt{2\kappa_2}\hat{a}_{\text{in},2},\end{aligned} \tag{3}$$

$$\dot{\hat{d}} = -(i\Delta_d + \gamma_d)\hat{d} + \sqrt{2}(ig^0_{\omega,d} - g^0_{\kappa,d})\hat{q}\hat{d} - \mathcal{G}\hat{a} - \sqrt{2}g^{0,+}_{a,d}\hat{q}\hat{a} + \left(\sqrt{2\gamma_d} + \frac{g^0_{\kappa,d}}{\sqrt{\gamma_d}}\hat{q}\right)(\alpha_{\text{las}} + \hat{a}_{\text{in},1}),$$

$$\dot{\hat{q}} = \Omega_{\text{m}}\hat{p},$$

$$\begin{aligned}\dot{\hat{p}} = &-\Omega_{\text{m}}\hat{q} - \gamma_{\text{m}}\hat{p} + i\sqrt{2}g^{0,-}_{a,d}(\hat{a}^\dagger\hat{d} - \hat{d}^\dagger\hat{a}) + \sqrt{2}g^0_{\omega,a}\hat{a}^\dagger\hat{a} + \sqrt{2}g^0_{\omega,d}\hat{d}^\dagger\hat{d} + \sqrt{\gamma_{\text{m}}}\hat{\xi} \\ &- i\frac{g^0_{\kappa,a}}{\sqrt{\kappa_1}}(\hat{a}^\dagger(\alpha_{\text{las}} + \hat{a}_{\text{in},1}) - (\alpha^*_{\text{las}} + \hat{a}^\dagger_{\text{in},1})\hat{a}) - i\frac{g^0_{\kappa,d}}{\sqrt{\gamma_d}}(\hat{d}^\dagger(\alpha_{\text{las}} + \hat{a}_{\text{in},1}) - (\alpha^*_{\text{las}} + \hat{a}^\dagger_{\text{in},1})\hat{d}).\end{aligned}$$

We have defined the detunings $\Delta_a = \omega_a - \omega_{\text{las}}$ and $\Delta_d = \omega_d - \omega_{\text{las}}$, the generalized coupling $\mathcal{G} = i\Lambda + \sqrt{\kappa_1\gamma_d}$, the total cavity loss rate $\kappa = \kappa_1 + \kappa_2$ and the effective optomechanical couplings

$$g^{0,\pm}_{a,d} = \frac{\sqrt{\kappa_1\gamma_d}}{2}\left(\frac{g^0_{\kappa,a}}{\kappa_1} \pm \frac{g^0_{\kappa,d}}{\gamma_d}\right). \tag{4}$$

At room temperature, we can neglect the thermal fluctuations in the optical environments, therefore $\hat{a}_{\text{in},\mu}$ corresponds to the vacuum input noise from environment $\mu = 1, 2$ and its only non-zero correlation function is $\langle\hat{a}_{\text{in},\mu}(t)\hat{a}^\dagger_{\text{in},\mu}(t')\rangle = \delta(t - t')$. Conversely, for the mechanical environment, this temperature is high, and the correlation function of the input mechanical noise $\hat{\xi}$ can be approximated by $\langle\hat{\xi}(t)\hat{\xi}(t')\rangle = (2\bar{n}_{\text{m}} + 1)\delta(t - t')$, where $\bar{n}_{\text{m}} = (\exp(\hbar\Omega_{\text{m}}/k_{\text{B}}T) - 1)^{-1}$ is the average phonon number in the mechanical environment.

Our microcavity is in the regime $g^0_{\omega,a}, g^0_{\omega,d}, g^0_{\kappa,a}, g^0_{\kappa,d} \ll \kappa, \gamma_d, \Lambda$ (see results section), so we can neglect the optomechanical effects when modeling the optical response of the cavity and, like in Ref. [38], we obtain the transmission coefficient of the cavity

$$t = \frac{\sqrt{2\kappa_2}\left(\sqrt{2\gamma_d}\mathcal{G} - \sqrt{2\kappa_1}(\gamma_d + i\Delta_d)\right)}{(\kappa + i\Delta_a)(\gamma_d + i\Delta_d) - \mathcal{G}^2}. \tag{5}$$

Furthermore, the cavity and PhC modes are in the strong coupling regime, $\Lambda > \gamma_d, \kappa$. We can thus estimate the effective optical resonances by diagonalizing the Langevin equations for the

Optics EXPRESS

average optical modes, in the absence of the mechanical resonator,

$$\begin{pmatrix} \langle \dot{\hat{a}} \rangle \\ \langle \dot{\hat{d}} \rangle \end{pmatrix} = -i \begin{pmatrix} \omega_a - i\kappa & -i\mathcal{G} \\ -i\mathcal{G} & \omega_d - i\gamma_d \end{pmatrix} \begin{pmatrix} \langle \hat{a} \rangle \\ \langle \hat{d} \rangle \end{pmatrix} + \begin{pmatrix} \sqrt{2\kappa_1}\alpha_{\mathrm{las}} \\ \sqrt{2\gamma_d}\alpha_{\mathrm{las}} \end{pmatrix}. \tag{6}$$

We obtain the complex eigenvalues

$$\tilde{\omega}_{\pm} = \frac{\omega_a + \omega_d}{2} - i\frac{\kappa + \gamma_d}{2} \pm \sqrt{\left(\frac{\omega_a - \omega_d}{2} - i\frac{\kappa - \gamma_d}{2}\right)^2 - \mathcal{G}^2}, \tag{7}$$

which correspond to the effective resonance frequencies $\omega_{\pm} = \Re(\tilde{\omega}_{\pm})$ and loss rates $\kappa_{\pm} = -\Im(\tilde{\omega}_{\pm})$. Since the optomechanical effects can be treated as a perturbation, we can simply introduce the mechanical position dependency of $\omega_a$, $\omega_d$, $\kappa_1$ and $\gamma_d$ in Eq. (7) and estimate the effective dispersive and dissipative couplings

$$g^0_{\omega,\pm} = -\frac{1}{\sqrt{2}}\partial\omega_{\pm}\partial q[q=0], \quad g^0_{\kappa,\pm} = \frac{1}{\sqrt{2}}\partial\kappa_{\pm}\partial q[q=0]. \tag{8}$$

Finally, given our laser power, the set of Eqs. (3) can be linearized around a semiclassical steady-state, allowing us to solve them and derive the mechanical frequency shift due to the optomechanical interactions, see Supplement 1 and Ref. [44].

## 4. Results

### 4.1. Optical properties of the microcavity

The optomechanical microcavity is formed by the PhC and DBR mirrors. While the stop-band of the DBR is determined by the heterostructure growth, the reflectance of the membrane can be engineered by the pattern of the PhC [25,26]. We use this flexibility to demonstrate the tunability of the microcavity resonance wavelength by only varying the radius of the PhC holes, without having to adjust the geometric length of the microcavity, i.e., the gap between the PhC and DBR mirrors. A change of the PhC parameters changes the effective length of the microcavity, $L_{\mathrm{eff}}$, which is given by the geometric cavity length, $L_{\mathrm{g}}$, and an additional length originating from the phase acquired by the light in the PhC and DBR mirrors [46]. We simulate the PhC membrane's reflectance using rigorous coupled wave analysis (RCWA) [24,47] to obtain the PhC parameters, i.e., PhC hole radius, $r_{\mathrm{PhC}}$, and PhC lattice constant, $a_{\mathrm{PhC}}$, such that the PhC yields its highest reflectance between 1480 nm to 1520 nm, which coincides with the reflectance band of the DBR.

Figure 3(a) shows the measured reflectance spectra of three fabricated microcavities with varied PhC hole radius and $a_{\mathrm{PhC}} = 1081$ nm. We observe three distinct features in these spectra, which we exemplarily discuss for the microcavity with a PhC hole radius of 367 nm. The microcavity resonance at 1508 nm appears as a pronounced minimum in the reflectance spectrum. It exhibits an optical quality factor of about $3 \cdot 10^2$ (corresponding to a Finesse of $3 \cdot 10^2$ as we work with the first half-wavelength mode in the microcavity). Its lineshape is slightly asymmetric due to the wavelength-dependent reflectance of the PhC slab [25,36]. Further, we observe a shallow reflectance dip at 1573 nm. This dip originates from light coupling to a parasitic guided resonance of the PhC membrane due to the finite waist of the laser beam [24,27]. Finally, two local minima at 1560 nm and 1600 nm are the first two transmission minima of the DBR mirror as confirmed by an independent measurement on a bare DBR (see Supplement 1).

In Fig. 3(c) we present simulation results of the optical response for microcavities with parameters as in Fig. 3(a). We obtain a good agreement between measurement and simulation for the features discussed above. However, we also observe discrepancies, such as a deviation in the depth of the microcavity resonance and DBR minima. We attribute these differences

Optics EXPRESS

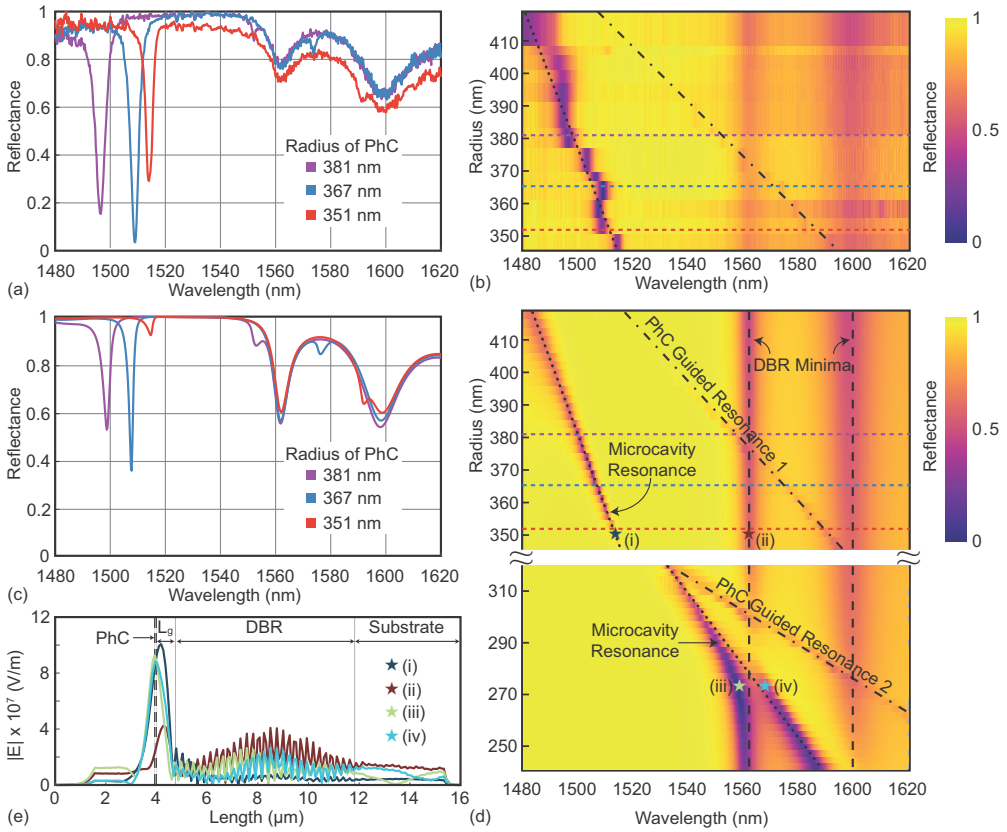


**Fig. 3.** Optical properties of the microcavity. (a) Reflectance spectra of a microcavity with PhC parameters: $a_{PhC}$ = 1081 nm, $r_{PhC}$ = 351, 367 and 381 nm. (b) Reflectance map of the microcavity for varying PhC radii. (c) Simulation of reflectance spectra of a microcavity with parameters as in (a). (d) Simulation of a reflectance map of the microcavity for various PhC radii. The dashed, dotted, and dotted-dashed lines represent the DBR minima, microcavity resonance, and parasitic PhC-guided resonances, respectively. (e) The electric field distribution $|E|$ in the microcavity and DBR at the points marked in (d).

to assumptions made in the RCWA simulation and approximations we make to simplify our model. The RCWA simulations assume a PhC that is in-plane infinitely periodic, while in the experiment, its size is given by the suspended area of the PhC membrane. Such finite-sized PhC structure reduces its absolute reflectance [48]. This reduced reflectance of the PhC membrane does not alter the cavity resonance wavelength but affects the reflectivity mismatch between the PhC and DBR mirrors, which determines the microcavity dip depth. Another difference stems from fabrication imperfections of the PhC pattern, where the PhC parameters slightly vary over the exposed area and the profile of the sidewall of the PhC hole slightly deviates from being perfectly vertical. The variation of the PhC hole radii on the same device will reduce the absolute reflectance and, thus, add another contribution to a reflectivity mismatch between the PhC and DBR mirror affecting the depth of the microcavity resonance. The deviation from the ideal vertical hole profile leads to an increase in the loss of the PhC guided resonance due to coupling between TE and TM modes inside the PhC slab [49,50], resulting in a change of the PhC reflectance. Note that absorption in the PhC or DBR would also impact the reflectivity match between the mirrors. We excite the microcavity below the bandgap of (Al,Ga)As and, thus,

Optics EXPRESS

exclude direct absorption. However, photons may still be absorbed through mid-gap states [51] or via two-photon processes [52]. In our case, we do not observe any nonlinear or thermally-induced optical lineshape change (see Supplement 1) and, thus, exclude a clear effect of absorption on the reflectivity mismatch. Finally, we attribute the discrepancy between the simulated and measured depth of the DBR minima to the non-uniform thickness of the grown GaAs and (Al,Ga)As layers of the DBR, which we assume to be perfectly uniform in the simulation. The non-uniform layer thickness will reduce the overall reflectivity of the DBR reflection band and will also result in an increase of the reflectance at the DBR minima outside of the reflection band (see Supplement 1).

To showcase the precise control over the microcavity resonance wavelength, we fabricated 14 devices with PhC hole radius varied from 351 nm to 420 nm and $a_{\mathrm{PhC}} = 1081$ nm on a single chip, whose measured and simulated reflectance spectra are shown in Fig. 3(b) and Fig. 3(d), respectively. We observe a clear trend of the microcavity resonance wavelength that increases at a rate of 0.49 nm per 1 nm decrease in PhC hole radius with a similar value of 0.45 nm per 1 nm for the simulated case. Note that we attribute the slight fluctuation in the microcavity position [see Fig. 3(b)] around the expected behavior [see Fig. 3(d)] to a fabrication-related uncertainty in the exact geometric length of the microcavity. We further observe that the wavelength of the parasitic guided resonance shifts to larger wavelengths with a decrease in PhC hole radius, as observed in Refs. [24,27,53,54], and captured in the simulation [see Fig. 3(d)].

Up until $r_{\mathrm{PhC}} = 310$ nm, the position of the two DBR minima is independent of the PhC hole radius. Upon further reduction of the PhC hole radius, the microcavity resonance approaches the first transmission minimum of the DBR mirror and an avoided crossing between the DBR minimum and the microcavity is observed. In general, the DBR reflection minima are eigenmodes of the DBR structure and have applications, for example, in distributed feedback lasers [55]. These reflection minima are a result of destructive interference of the electric field in the DBR layers such that light is perfectly transmitted. In the presence of the microcavity field, the interference effect is disturbed, leading to the formation of new eigenmodes. To examine these new eigenmodes, we simulated the electric field distribution for a PhC hole radius of 275 nm at the two branches of the avoided crossing, see Fig. 3(e). Similarly, the electric field distribution of the microcavity mode and the eigenmode of the DBR far away from the avoided crossing for a PhC hole radius of 350 nm is simulated for comparison. At the PhC hole radius of 350 nm and at the microcavity resonance (i), the electric field is predominantly concentrated in the PhC membrane and vacuum gap. The DBR eigenmode at a PhC hole radius of 350 nm (ii) is mostly contained in the DBR. At the avoided crossing (iii-iv), we observe that the microcavity and DBR eigenmode couple, and the energy is distributed between (i) and (ii) modes. This mode coupling is very similar to a system analyzed in Ref. [56], which studied the coupling between an out-of-plane microcavity and an in-plane distributed feedback laser. The observed avoided crossing could have interesting applications in optomechanics. For example, one could functionalize the DBR layers by using lasing-active materials such that the optomechanical microcavity could be internally optically pumped [57,58].

### 4.2. Mechanical properties of the suspended PhC membrane

We now turn to the characterization of the mechanical properties of the suspended PhC membrane. Figure 4(a) shows a representative displacement noise power spectrum of a circular PhC membrane with a diameter of 100 $\mu$m. The fundamental mechanical mode is observed at 528 kHz and the first higher order mode at 834 kHz. We attribute the modes through measurements of the spatially-dependent mode displacement recorded via mechanical mode tomography [24], shown in the insets of Fig. 4(a). The observed mode shapes reflect the expected behavior of a circular membrane and, thus, prove a complete and clean release of the PhC membrane on top of the 750 nm air gap over the DBR mirror. When decreasing the diameter of the released PhC membrane, we observe an increase in the mechanical resonance frequency, see Fig. 4(b). While

Optics EXPRESS

the variation of the PhC hole radius has a large impact on the optical resonance wavelength of the microcavity, we observe in Fig. 4(b) that the mechanical frequency of the fundamental mode only slightly decreases with an increase in PhC hole radius. This behavior is anticipated as the mechanical frequency is proportional to the ratio of the stiffness and mass of the PhC membrane, which both increase with a decrease in PhC hole radius, thus, leading to only a slight change in mechanical frequency. To confirm this observation, we performed FEM simulations of the PhC membranes [dashed line in Fig. 4(b)], whose results reflect the experimental measurements when assuming an initial tensile stress of 45 MPa in the device layer [24] (see Supplement 1).

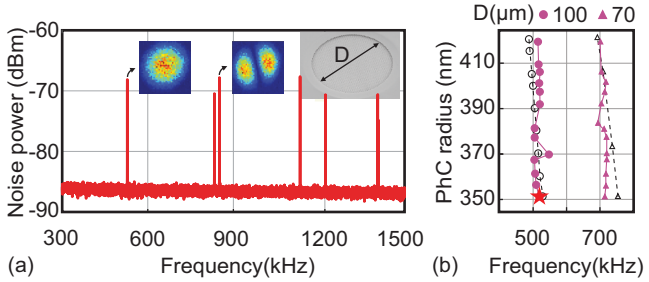


**Fig. 4.** Mechanical eigenfrequencies of the suspended PhC membrane. (a) Displacement noise power spectrum (NPS) of the thermally driven mechanical motion of a membrane of diameter 100 $\mu$m (SEM image in the top right corner). The insets show the recorded mechanical mode tomography of the first two mechanical eigenmodes. (b) Measured frequencies of the fundamental mode of PhC membranes of two different diameters, where $r_{\mathrm{PhC}}$ is varied. The triangles (circles) represent PhC mirrors with a diameter of 70 $\mu$m (100 $\mu$m). The red star marks the device whose NPS is presented in (a). The black triangles (circles) show the frequencies of the fundamental mode of 70 $\mu$m (100 $\mu$m) PhC mirrors simulated via FEM. Lines are a guide to the eye.

We also measured the mechanical quality factor $Q_{\mathrm{m}}$ via ringdown measurements and obtain values of $\leq 3 \cdot 10^4$. Note that $Q_{\mathrm{m}}$ can be vastly increased by substituting GaAs with tensile-strained InGaP [59–61], which is fully compatible with the presented monolithic (Al,Ga)As heterostructure growth and microfabrication process. High tensile stress in high aspect ratio nanomechanical resonators gives rise to large dissipation dilution (e.g. via the use of thin millimeter-sized trampoline-shaped resonators [61–64]) that can drastically increase $Q_{\mathrm{m}}$, which can be further increased by mode-shape engineering, i.e., soft-clamping and strain engineering [62,65,66]. Furthermore, the use of tensile-strained materials would allow the fabrication of a PhC with a larger area, which would eliminate diffraction loss.

### 4.3. *Microcavity optomechanics*

The mechanical properties of the suspended PhC mirror can be altered by the interaction of its motion with the microcavity field. Figure 5 shows the displacement noise power spectrum (NPS) of the fundamental mode of the suspended PhC mirror in dependence on the wavelength of the incident laser light. We clearly observe a non-symmetric mechanical frequency shift with respect to the microcavity resonance, which is predominantly to smaller frequencies. These features are also present in other devices, where we vary the PhC hole radius. In the presented device, the maximal shift of about $-400$ Hz occurs at a pump wavelength of 1505 nm, which is 3 nm red-detuned with respect to the microcavity resonance. Such characteristics are not expected from the optical spring effect in non-sideband resolved canonical optomechanics [9]. When increasing the input power to the microcavity, we observe that the mechanical frequency shift increases accordingly (see Supplement 1). We verified that the optical reflectivity of the microcavity is not dependent on the optical input power (see Supplement 1), which allows us

Optics EXPRESS

to exclude nonlinear optical effects [67,68]. Heating of the PhC membrane through absorption would lead to a change of the optical lineshape, which we do not observe, and also to a shift of the mechanical frequency. The latter we can rule out for another sample (see Supplement 1), where the mechanical frequency far off-resonant of the microcavity is largely unaffected by optical power.

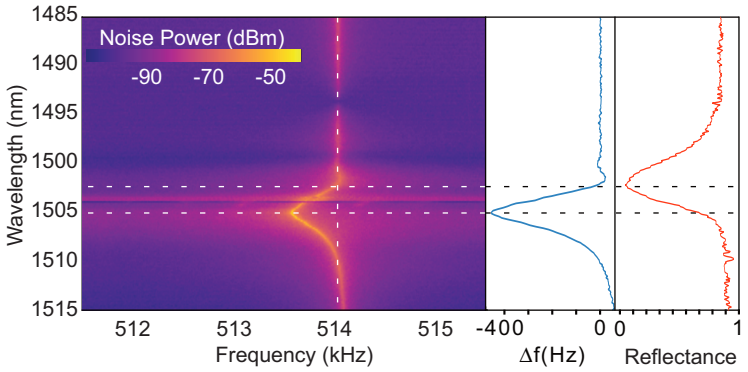


**Fig. 5.** Microcavity optomechanics. The thermally driven noise power spectrum of the fundamental mode of the suspended PhC membrane shows a pronounced frequency shift for laser detunings that are red-detuned with respect to the microcavity resonance. The panel on the right shows the optical reflectance of the microcavity and the extracted mechanical frequency shift of the mechanical mode. The horizontal lines indicate the optical cavity resonance and the wavelength of the maximal mechanical frequency shift.

As outlined in the theory section, we account for dispersive and dissipative couplings of the mechanical mode of the suspended PhC to the Fabry-Perot-type mode of the microcavity and to the guided mode of the PhC. Figure 6(a) shows a combined fit of our model to the data of the optical reflectivity and of the mechanical frequency shift. We observe that we can reproduce the asymmetric optical lineshape and the off-resonant frequency shift of the mechanics. Figure 6(b) shows the mechanical frequency shift, when we switch off all but one coupling. We observe that the shifts from individual couplings alone do not add up to the full mechanical frequency shift from panel (a) because of the presence of cross-terms involving different kinds of optomechanical couplings (see Supplement 1) and none of the individual couplings can capture well the observed frequency shift. Fig. 6(c) presents the mechanical frequency shift, when we switch off either the dissipative or the dispersive couplings, but leave the other ones on. We observe that the dispersive coupling captures the experimental behavior to a great extent, while the dissipative coupling yields a small correction. The major contribution comes from $g^0_{\omega,d}$ while the one from $g^0_{\kappa,a}$ is negligible.

Importantly, we find that the optical coupling $\Lambda$ between the cavity mode $\hat{a}$ and PhC mode $\hat{d}$ is in the strong coupling regime, $\Lambda > \kappa, \gamma_d$, while the optomechanical couplings $g^0_i$ can be treated as a perturbation. We attribute this strong optical coupling to the hybridization of the PhC-guided resonance and the Fabry-Perot-type mode [see the electric field in Fig. 1(d)]. Therefore, using Eq. (7), we determine that the effective resonances of the microcavity are at wavelengths $\lambda_+ = 1444\,\text{nm}$ and $\lambda_- = 1503\,\text{nm}$ and the corresponding loss rates are $\kappa_+/2\pi = 6.01\,\text{THz}$ and $\kappa_-/2\pi = 277\,\text{GHz}$, respectively. The values of $\lambda_-$ and $\kappa_-$ are in good agreement with the experimental results shown in Fig. 6(a) and are associated with the effective optomechanical couplings $g^0_{\omega,-}/2\pi = -496\,\text{kHz}$ and $g^0_{\kappa,-}/2\pi = 33.3\,\text{kHz}$, see Eq. (8). Note that the mode at $\lambda_+$ is extremely lossy and, thus, will be difficult to be observed experimentally.

Optics EXPRESS

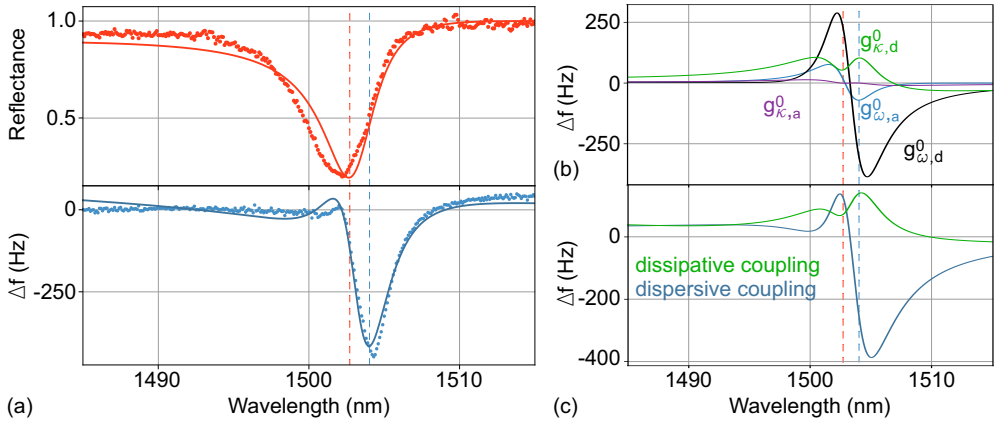


**Fig. 6.** (a) Microcavity reflectance (top panel) and frequency shift (bottom panel). Theoretical values are presented in solid lines and experimental ones in dots. For this plot $\gamma_d/2\pi = 3.8\,\mathrm{THz}$, $\lambda_d = 1473\,\mathrm{nm}$, $\Omega_\mathrm{m}/2\pi = 514\,\mathrm{kHz}$, $\lambda_a/2\pi = 1473.3\,\mathrm{nm}$, $\kappa_1/2\pi = 2.12\,\mathrm{THz}$, $\kappa_2/2\pi = 366\,\mathrm{GHz}$, $\Lambda/2\pi = 4.09\,\mathrm{THz}$. Coupling strengths $g^0_{\kappa,a}/2\pi = 775\,\mathrm{kHz}$, $g^0_{\kappa,d}/2\pi = 3.21\,\mathrm{MHz}$, $g^0_{\omega,a}/2\pi = 845\,\mathrm{kHz}$, $g^0_{\omega,d}/2\pi = -1.82\,\mathrm{MHz}$. (b),(c) Comparison of coupling strength contributions to the frequency shift: (b) contribution of individual coupling (no cross-terms are taken into account), (c) only dissipative ($g^0_{\kappa,a}$ and $g^0_{\kappa,d}$) or dispersive ($g^0_{\omega,a}$ and $g^0_{\omega,d}$) coupling are considered. The vertical dashed lines denote the microcavity resonance (red) and wavelength of maximal mechanical frequency shift (blue).

Importantly, we can connect the fitted parameters from Fig. 6 to parameters that are accessible from the experiment or simulations. We outline this procedure in the Supplement 1. We find reasonable experimental values for most of these parameters. An important quantity is the dominating coupling strength, $g^0_{\omega,-}/2\pi$, which we determine as a moving boundary coupling of the mechanical motion of the PhC to the microcavity optical field by FEM simulations [69,70] (see Supplement 1, Table S2). We obtain a simulated value that is wavelength-dependent and that is maximally $\sim -2\pi \cdot 240\,\mathrm{kHz}$. This value is only about a factor of two smaller than the value we obtain from the fit.

To further characterize the microcavity, a desired feature would be to tune the vacuum gap between the PhC and DBR mirrors. This gap impacts the optomechanical coupling strength and character as it will modify the coupling strength between the PhC guided mode and the Fabry-Perot mode. This gap could be tuned in-situ in a monolithic structure by using electrostatic tuning as is done, for example, in VCSELs [71–73], or could be realized by the growth of wafers with varying sacrificial layer thickness. Alternatively, a change of the parameters of the PhC pattern will impact the strength of the couplings as well and could be used for a systematic study thereof.

## 5. Conclusions and outlook

We demonstrated an on-chip free-space optomechanical microcavity of sub-wavelength length monolithically fabricated from an (Al,Ga)As heterostructure. We showed the tunability of the cavity resonance wavelength by a simple change of the radius of the PhC holes. We found that the microcavity mode and transmissive modes of the DBR can strongly couple, which may offer new applications in the field of optomechancis, for example, by incorporating active lasing materials within the DBR. The interplay between the Fabry-Perot mode and the guided resonance of the suspended PhC resulted in a modified optomechanical response, which we modeled by

Optics EXPRESS

accounting for dispersive and dissipative optomechanical couplings. Future studies with variable gaps are required to separate these couplings clearly from each other.

The presented optomechanical microcavity is amenable for optomechanical state preparation protocols, such as efficient cooling [38] or squeezed mechanical state generation [74]. The latter protocol exploits the ultrastrong coupling regime [75], which our microcavity accesses, but any effects of that regime are currently masked by the large optical decay rate. Our approach allows for a smooth integration of multiple suspended PhC slabs and, thus, the realization of multi-element optomechanics [76] on chip, which has been proposed to achieve the elusive single-photon strong coupling regime [77,78]. Additionally, our approach would enable the realization of arrays of optomechanical microcavities on a single chip with applications in sensing and optical networks [20]. Finally, by use of the concept of bound states in the continuum realized with multiple PhC slabs [37], it is possible to drastically reduce optical loss, which is the current roadblock in achieving strong optomechanical coupling physics.

**Funding.** Knut och Alice Wallenbergs Stiftelse (Wallenberg Academy Fellowship, Wallenberg Center for Quantum Technology); QuantERA (C'MON-QSENS!); Vetenskapsrådet (2018-05061, 2018-05973, 2019-00390, 2019-04946, 2022-06725); HORIZON EUROPE Marie Sklodowska-Curie Actions (MSCA-PF-2022-OCOMM).

**Acknowledgments.** This work was partially supported by Chalmers' Area of Advance Nano. Samples were fabricated in the Myfab Nanofabrication Laboratory at Chalmers and analyzed in the Chalmers Materials Analysis Laboratory. Simulations were performed on resources provided by the National Academic Infrastructure for Supercomputing in Sweden (NAISS) and the Swedish National Infrastructure for Computing (SNIC) at Tetralith.

We acknowledge the group of Victor Torres Company for their support with a tunable telecom laser, and Joachim Ciers for fruitful discussions.

**Disclosures.** The authors declare no conflicts of interest.

**Data availability.** Data underlying the results presented in this paper are available in the open-access Zenodo database [79].

**Supplemental document.** See Supplement 1 for supporting content.

## References

1. K. J. Vahala, "Optical microcavities," Nature **424**(6950), 839–846 (2003).
2. D. Najer, I. Söllner, P. Sekatski, V. Dolique, M. C. Löbl, D. Riedel, R. Schott, S. Starosielec, S. R. Valentin, A. D. Wieck, N. Sangouard, A. Ludwig, and R. J. Warburton, "A gated quantum dot strongly coupled to an optical microcavity," Nature **575**(7784), 622–627 (2019).
3. R. Albrecht, A. Bommer, C. Deutsch, J. Reichel, and C. Becher, "Coupling of a single nitrogen-vacancy center in diamond to a fiber-based microcavity," Phys. Rev. Lett. **110**(24), 243602 (2013).
4. J. P. Reithmaier, G. Sek, A. Löffler, C. Hofmann, S. Kuhn, S. Reitzenstein, L. V. Keldysh, V. D. Kulakovskii, T. L. Reinecke, and A. Forchel, "Strong coupling in a single quantum dot–semiconductor microcavity system," Nature **432**(7014), 197–200 (2004).
5. G. Lin, A. Coillet, and Y. K. Chembo, "Nonlinear photonics with high-q whispering-gallery-mode resonators," Adv. Opt. Photonics **9**(4), 828–890 (2017).
6. T. J. Kippenberg, S. M. Spillane, and K. J. Vahala, "Kerr-nonlinearity optical parametric oscillation in an ultrahigh-$q$ toroid microcavity," Phys. Rev. Lett. **93**(8), 083904 (2004).
7. R. Michalzik, ed., *VCSELs*, vol. 166 of *Springer Series in Optical Sciences* (Springer Berlin Heidelberg, 2013).
8. L. He, S. K. Özdemir, and L. Yang, "Whispering gallery microcavity lasers," Laser Photonics Rev. **7**(1), 60–82 (2013).
9. M. Aspelmeyer, T. J. Kippenberg, and F. Marquardt, "Cavity optomechanics," Rev. Mod. Phys. **86**(4), 1391–1452 (2014).
10. J. Chan, T. P. M. Alegre, A. H. Safavi-Naeini, J. T. Hill, A. Krause, S. Gröblacher, M. Aspelmeyer, and O. Painter, "Laser cooling of a nanomechanical oscillator into its quantum ground state," Nature **478**(7367), 89–92 (2011).
11. J. D. Teufel, T. Donner, D. Li, J. W. Harlow, M. S. Allman, K. Cicak, A. J. Sirois, J. D. Whittaker, K. W. Lehnert, and R. W. Simmonds, "Sideband cooling of micromechanical motion to the quantum ground state," Nature **475**(7356), 359–363 (2011).
12. S. Gröblacher, K. Hammerer, M. R. Vanner, and M. Aspelmeyer, "Observation of strong coupling between a micromechanical resonator and an optical cavity field," Nature **460**(7256), 724–727 (2009).
13. E. Verhagen, S. Deléglise, S. Weis, A. Schliesser, and T. J. Kippenberg, "Quantum-coherent coupling of a mechanical oscillator to an optical cavity mode," Nature **482**(7383), 63–67 (2012).
14. R. Leijssen, G. R. La Gala, L. Freisem, J. T. Muhonen, and E. Verhagen, "Nonlinear cavity optomechanics with nanomechanical thermal fluctuations," Nat. Commun. **8**(1), ncomms16024 (2017).

Optics EXPRESS


15. X. Jiang, Q. Lin, J. Rosenberg, K. Vahala, and O. Painter, "High-q double-disk microcavities for cavity optomechanics," Opt. Express **17**(23), 20911–20919 (2009).
16. M. Eichenfield, J. Chan, R. M. Camacho, K. J. Vahala, and O. Painter, "Optomechanical crystals," Nature **462**(7269), 78–82 (2009).
17. L. Ding, C. Baker, P. Senellart, A. Lemaitre, S. Ducci, G. Leo, and I. Favero, "High frequency gaas nano-optomechanical disk resonator," Phys. Rev. Lett. **105**(26), 263903 (2010).
18. J. Hofer, A. Schliesser, and T. J. Kippenberg, "Cavity optomechanics with ultrahigh-$q$ crystalline microresonators," Phys. Rev. A **82**(3), 031804 (2010).
19. V. Tsvirkun, A. Surrente, F. Raineri, G. Beaudoin, R. Raj, I. Sagnes, I. Robert-Philip, and R. Braive, "Integrated III-V Photonic Crystal – Si waveguide platform with tailored optomechanical coupling," Sci. Rep. **5**(1), 16526 (2015).
20. G. Wachter, S. Kuhn, S. Minniberger, C. Salter, P. Asenbaum, J. Millen, M. Schneider, J. Schalko, U. Schmid, A. Felgner, D. Hüser, M. Arndt, and M. Trupke, "Silicon microcavity arrays with open access and a finesse of half a million," Light: Sci. Appl. **8**(1), 37 (2019).
21. G. J. Hornig, S. Al-Sumaidae, J. Maldaner, L. Bu, and R. G. DeCorby, "Monolithically integrated membrane-in-the-middle cavity optomechanical systems," Opt. Express **28**(19), 28113–28125 (2020).
22. H. Pfeifer, L. Ratschbacher, J. Gallego, C. Saavedra, A. Faßbender, A. von Haaren, W. Alt, S. Hofferberth, M. Köhl, S. Linden, and D. Meschede, "Achievements and perspectives of optical fiber Fabry–Perot cavities," Appl. Phys. B **128**(2), 29 (2022).
23. S. M. Meenehan, J. D. Cohen, S. Gröblacher, J. T. Hill, A. H. Safavi-Naeini, M. Aspelmeyer, and O. Painter, "Silicon optomechanical crystal resonator at millikelvin temperatures," Phys. Rev. A **90**(1), 011803 (2014).
24. S. Kini Manjeshwar, K. Elkhouly, J. M. Fitzgerald, M. Ekman, Y. Zhang, F. Zhang, S. M. Wang, P. Tassin, and W. Wieczorek, "Suspended photonic crystal membranes in algaas heterostructures for integrated multi-element optomechanics," Appl. Phys. Lett. **116**(26), 264001 (2020).
25. S. Fan and J. D. Joannopoulos, "Analysis of guided resonances in photonic crystal slabs," Phys. Rev. B **65**(23), 235112 (2002).
26. K. Makles, T. Antoni, A. G. Kuhn, S. Deléglise, T. Briant, P.-F. Cohadon, R. Braive, G. Beaudoin, L. Pinard, C. Michel, V. Dolique, R. Flaminio, G. Cagnoli, I. Robert-Philip, and A. Heidmann, "2D photonic-crystal optomechanical nanoresonator," Opt. Lett. **40**(2), 174–177 (2015).
27. J. P. Moura, R. A. Norte, J. Guo, C. Schäfermeier, and S. Gröblacher, "Centimeter-scale suspended photonic crystal mirrors," Opt. Express **26**(2), 1895–1909 (2018).
28. C. H. Bui, J. Zheng, S. W. Hoch, L. Y. T. Lee, J. G. E. Harris, and C. Wei Wong, "High-reflectivity, high-q micromechanical membranes via guided resonances for enhanced optomechanical coupling," Appl. Phys. Lett. **100**(2), 021110 (2012).
29. A. W. Rodriguez, A. P. McCauley, P.-C. Hui, D. Woolf, E. Iwase, F. Capasso, M. Loncar, and S. G. Johnson, "Bonding, antibonding and tunable optical forces in asymmetric membranes," Opt. Express **19**(3), 2225–2241 (2011).
30. D. Woolf, P.-C. Hui, E. Iwase, M. Khan, A. W. Rodriguez, P. Deotare, I. Bulu, S. G. Johnson, F. Capasso, and M. Loncar, "Optomechanical and photothermal interactions in suspended photonic crystal membranes," Opt. Express **21**(6), 7258–7275 (2013).
31. X. Chen, C. Chardin, K. Makles, C. Caër, S. Chua, R. Braive, I. Robert-Philip, T. Briant, P.-F. Cohadon, A. Heidmann, T. Jacqmin, and S. Deléglise, "High-finesse Fabry–Perot cavities with bidimensional Si3N4 photonic-crystal slabs," Light: Sci. Appl. **6**(1), e16190 (2016).
32. C. Gärtner, J. P. Moura, W. Haaxman, R. A. Norte, and S. Gröblacher, "Integrated optomechanical arrays of two high reflectivity sin membranes," Nano Lett. **18**(11), 7171–7175 (2018).
33. F. Zhou, Y. Bao, J. J. Gorman, and J. Lawall, "Cavity optomechanical bistability with an ultrahigh reflectivity photonic crystal membrane," arXiv, 2211.10485 (2022).
34. G. Enzian, Z. Wang, A. Simonsen, J. Mathiassen, T. Vibel, Y. Tsaturyan, A. Tagantsev, A. Schliesser, and E. S. Polzik, "Phononically shielded photonic-crystal mirror membranes for cavity quantum optomechanics," Opt. Express **31**(8), 13040–13052 (2023).
35. J. Guo, R. A. Norte, and S. Gröblacher, "Integrated optical force sensors using focusing photonic crystal arrays," Opt. Express **25**(8), 9196–9203 (2017).
36. A. Naesby and A. Dantan, "Microcavities with suspended subwavelength structured mirrors," Opt. Express **26**(23), 29886–29894 (2018).
37. J. M. Fitzgerald, S. K. Manjeshwar, W. Wieczorek, and P. Tassin, "Cavity optomechanics with photonic bound states in the continuum," Phys. Rev. Res. **3**(1), 013131 (2021).
38. O. Černotík, A. Dantan, and C. Genes, "Cavity Quantum Electrodynamics with Frequency-Dependent Reflectors," Phys. Rev. Lett. **122**(24), 243601 (2019).
39. A. Xuereb, R. Schnabel, and K. Hammerer, "Dissipative Optomechanics in a Michelson-Sagnac Interferometer," Phys. Rev. Lett. **107**(21), 213604 (2011).
40. J. Baraillon, B. Taurel, P. Labeye, and L. Duraffourg, "Linear analytical approach to dispersive, external dissipative, and intrinsic dissipative couplings in optomechanical systems," Phys. Rev. A **102**(3), 033509 (2020).
41. D. Hunger, T. Steinmetz, Y. Colombe, C. Deutsch, T. W. Hänsch, and J. Reichel, "A fiber Fabry-Perot cavity with high finesse," New J. Phys. **12**(6), 065038 (2010).

Optics EXPRESS


42. P. Qing, J. Gong, X. Lin, N. Yao, W. Shen, A. Rahimi-Iman, W. Fang, and L. Tong, "A simple approach to fiber-based tunable microcavity with high coupling efficiency," Appl. Phys. Lett. **114**(2), 021106 (2019).
43. A. Barg, Y. Tsaturyan, E. Belhage, W. H. Nielsen, C. B. Møller, and A. Schliesser, "Measuring and imaging nanomechanical motion with laser light," Appl. Phys. B **123**(1), 8 (2017).
44. J. Monsel, A. Ciers, S. Kini Manjeshwar, W. Wieczorek, and J. Splettstoesser, "Dissipative and dispersive optomechanics with a frequency-dependent mirror," In preparation.
45. F. Elste, S. M. Girvin, and A. A. Clerk, "Quantum Noise Interference and Backaction Cooling in Cavity Nanomechanics," Phys. Rev. Lett. **102**(20), 207209 (2009).
46. J. H. E. Kim, L. Chrostowski, E. Bisaillon, and D. V. Plant, "DBR, sub-wavelength grating, and photonic crystal slab Fabry-Perot cavity design using phase analysis by FDTD," Opt. Express **15**(16), 10330–10339 (2007).
47. V. Liu and S. Fan, "S4: A free electromagnetic solver for layered periodic structures," Comput. Phys. Commun. **183**(10), 2233–2244 (2012).
48. D. K. Jacob, S. C. Dunn, and M. G. Moharam, "Design considerations for narrow-band dielectric resonant grating reflection filters of finite length," J. Opt. Soc. Am. A **17**(7), 1241–1249 (2000).
49. Y. Tanaka, T. Asano, Y. Akahane, B.-S. Song, and S. Noda, "Theoretical investigation of a two-dimensional photonic crystal slab with truncated cone air holes," Appl. Phys. Lett. **82**(11), 1661–1663 (2003).
50. U. K. Khankhoje, S.-H. Kim, B. C. Richards, J. Hendrickson, J. Sweet, J. D. Olitzky, G. Khitrova, H. M. Gibbs, and A. Scherer, "Modelling and fabrication of GaAs photonic-crystal cavities for cavity quantum electrodynamics," Nanotechnology **21**(6), 065202 (2010).
51. B. Guha, F. Marsault, F. Cadiz, L. Morgenroth, V. Ulin, V. Berkovitz, A. Lemaître, C. Gomez, A. Amo, S. Combrié, B. Gérard, G. Leo, and I. Favero, "Surface-enhanced gallium arsenide photonic resonator with quality factor of $6\times10^6$," Optica **4**(2), 218–221 (2017).
52. C. Yang, A. Villeneuve, G. Stegeman, C.-H. Lin, and H.-H. Lin, "Anisotropic two-photon transitions in GaAs/AlGaAs multiple quantum well waveguides," IEEE J. Quantum Electron. **29**(12), 2934–2939 (1993).
53. A. Singh Chadha, D. Zhao, S. Chuwongin, Z. Ma, and W. Zhou, "Polarization- and angle-dependent characteristics in two dimensional photonic crystal membrane reflectors," Appl. Phys. Lett. **103**(21), 211107 (2013).
54. S. Bernard, C. Reinhardt, V. Dumont, Y.-A. Peter, and J. C. Sankey, "Precision resonance tuning and design of sin photonic crystal reflectors," Opt. Lett. **41**(24), 5624–5627 (2016).
55. H. Ghafouri-Shiraz, *Distributed Feedback Laser Diodes and Optical Tunable Filters* (Wiley, 2004).
56. L. Mahler, A. Tredicucci, F. Beltram, H. E. Beere, and D. A. Ritchie, "Tuning a distributed feedback laser with a coupled microcavity," Opt. Express **18**(18), 19185–19191 (2010).
57. W. Yang, S. A. Gerke, K. W. Ng, Y. Rao, C. Chase, and C. J. Chang-Hasnain, "Laser optomechanics," Sci. Rep. **5**(1), 13700 (2015).
58. D. Yu and F. Vollmer, "Active optomechanics," Commun. Phys. **5**(1), 61 (2022).
59. G. D. Cole, P.-L. Yu, C. Gärtner, K. Siquans, R. Moghadas Nia, J. Schmöle, J. Hoelscher-Obermaier, T. P. Purdy, W. Wieczorek, C. A. Regal, and M. Aspelmeyer, "Tensile-strained inxga1-xp membranes for cavity optomechanics," Appl. Phys. Lett. **104**(20), 201908 (2014).
60. M. Bückle, V. C. Hauber, G. D. Cole, C. Gärtner, U. Zeimer, J. Grenzer, and E. M. Weig, "Stress control of tensile-strained In1-xGaxP nanomechanical string resonators," Appl. Phys. Lett. **113**(20), 201903 (2018).
61. S. K. Manjeshwar, A. Ciers, F. Hellman, J. Bläsing, A. Strittmatter, and W. Wieczorek, "High-Q Trampoline Resonators from Strained Crystalline InGaP for Integrated Free-Space Optomechanics," Nano Lett. **23**(11), 5076–5082 (2023).
62. R. A. Norte, J. P. Moura, and S. Gröblacher, "Mechanical resonators for quantum optomechanics experiments at room temperature," Phys. Rev. Lett. **116**(14), 147202 (2016).
63. C. Reinhardt, T. Müller, A. Bourassa, and J. C. Sankey, "Ultralow-noise sin trampoline resonators for sensing and optomechanics," Phys. Rev. X **6**(2), 021001 (2016).
64. E. Romero, V. M. Valenzuela, A. R. Kermany, L. Sementilli, F. Iacopi, and W. P. Bowen, "Engineering the dissipation of crystalline micromechanical resonators," Phys. Rev. Appl. **13**(4), 044007 (2020).
65. Y. Tsaturyan, A. Barg, E. S. Polzik, and A. Schliesser, "Ultracoherent nanomechanical resonators via soft clamping and dissipation dilution," Nat. Nanotechnol. **12**(8), 776–783 (2017).
66. A. H. Ghadimi, S. A. Fedorov, N. J. Engelsen, M. J. Bereyhi, R. Schilling, D. J. Wilson, and T. J. Kippenberg, "Elastic strain engineering for ultralow mechanical dissipation," Science **360**(6390), 764–768 (2018).
67. S. Combrié, A. D. Rossi, Q. V. Tran, and H. Benisty, "GaAs photonic crystal cavity with ultrahigh $Q$: Microwatt nonlinearity at 1.55 $\mu$m," Opt. Lett. **33**(16), 1908–1910 (2008).
68. D. Parrain, C. Baker, G. Wang, B. Guha, E. G. Santos, A. Lemaitre, P. Senellart, G. Leo, S. Ducci, and I. Favero, "Origin of optical losses in gallium arsenide disk whispering gallery resonators," Opt. Express **23**(15), 19656–19672 (2015).
69. S. G. Johnson, M. Ibanescu, M. A. Skorobogatiy, O. Weisberg, J. D. Joannopoulos, and Y. Fink, "Perturbation theory for Maxwell's equations with shifting material boundaries," Phys. Rev. E **65**(6), 066611 (2002).
70. J. Chan, A. H. Safavi-Naeini, J. T. Hill, S. Meenehan, and O. Painter, "Optimized optomechanical crystal cavity with acoustic radiation shield," Appl. Phys. Lett. **101**(8), 081115 (2012).
71. G. Cole, E. Bjorlin, Q. Chen, C.-Y. Chan, S. Wu, C. Wang, N. MacDonald, and J. Bowers, "MEMS-tunable vertical-cavity SOAs," IEEE J. Quantum Electron. **41**(3), 390–407 (2005).

Optics EXPRESS


72. S. Boutami, B. B. Bakir, J.-L. Leclercq, X. Letartre, P. Rojo-Romeo, M. Garrigues, P. Viktorovitch, I. Sagnes, L. Legratiet, and M. Strassner, "Highly selective and compact tunable MOEMS photonic crystal Fabry-Perot filter," Opt. Express **14**(8), 3129–3137 (2006).
73. M. C. Y. Huang, Y. Zhou, and C. J. Chang-Hasnain, "A nanoelectromechanical tunable laser," Nat. Photonics **2**(3), 180–184 (2008).
74. K. Kustura, C. Gonzalez-Ballestero, A. de los Ríos Sommer, N. Meyer, R. Quidant, and O. Romero-Isart, "Mechanical Squeezing via Unstable Dynamics in a Microcavity," Phys. Rev. Lett. **128**(14), 143601 (2022).
75. K. Dare, J. J. Hansen, I. Coroli, A. Johnson, M. Aspelmeyer, and U. Delić, "Linear Ultrastrong Optomechanical Interaction," arXiv, 2305.16226 (2023).
76. A. Xuereb, C. Genes, and A. Dantan, "Collectively enhanced optomechanical coupling in periodic arrays of scatterers," Phys. Rev. A **88**(5), 053803 (2013).
77. P. Rabl, "Photon Blockade Effect in Optomechanical Systems," Phys. Rev. Lett. **107**(6), 063601 (2011).
78. A. Nunnenkamp, K. Børkje, and S. M. Girvin, "Single-Photon Optomechanics," Phys. Rev. Lett. **107**(6), 063602 (2011).
79. S. Kini Manjeshwar, A. Ciers, J. Monsel, H. Pfeifer, C. Peralle, S. M. Wang, P. Tassin, and W. Wieczorek, "Data for "Integrated microcavity optomechanics with a suspended photonic crystal mirror above a distributed Bragg reflector"," Zenodo (2023), https://doi.org/10.5281/zenodo.7992175.